Buried amorphous layers by electronic excitation in ion-beam irradiated lithium niobate: Structure and kinetics

J. Olivares, A. García-Navarro, G. García, F. Agulló-López, F. Agulló-Rueda et al.

Citation: J. Appl. Phys. **101**, 033512 (2007); doi: 10.1063/1.2434801

View online: http://dx.doi.org/10.1063/1.2434801

View Table of Contents: http://jap.aip.org/resource/1/JAPIAU/v101/i3

Published by the American Institute of Physics.

Buried amorphous layers by electronic excitation in ion-beam irradiated lithium niobate: Structure and kinetics

J. Olivares[a)]
Instituto de Óptica, CSIC, C/Serrano 121, E-28006 Madrid, Spain

A. García-Navarro, G. García,[b)] and F. Agulló-López[c)]
Centro de Microanálisis de Materiales (CMAM), Universidad Autónoma de Madrid, E-28049 Madrid, Spain

F. Agulló-Rueda
Instituto de Ciencia de Materiales de Madrid (ICMM), CSIC, Campus de Cantoblanco, E-28049 Madrid, Spain

A. García-Cabañes and M. Carrascosa
Departamento de Física de Materiales C-IV, Universidad Autónoma de Madrid, E-28049 Madrid, Spain

(Received 17 July 2006; accepted 4 December 2006; published online 7 February 2007)

The formation of buried heavily damaged and amorphous layers by a variety of swift-ion irradiations (F at 22 MeV, O at 20 MeV, and Mg at 28 MeV) on congruent $LiNbO_3$ has been investigated. These irradiations assure that the electronic stopping power $S_e(z)$ is dominant over the nuclear stopping $S_n(z)$ and reaches a maximum value inside the crystal. The structural profile of the irradiated layers has been characterized in detail by a variety of spectroscopic techniques including dark-mode propagation, micro-Raman scattering, second-harmonic generation, and Rutherford backscattering spectroscopy/channeling. The growth of the damage on increasing irradiation fluence presents two differentiated stages with an *abrupt structural transition* between them. The heavily damaged layer reached as a *final stage* is optically isotropic (refractive index $n=2.10$, independent of bombarding ion) and has an *amorphous* structure. Moreover, it has sharp profiles and its thickness progressively increases with irradiation fluence. The dynamics under irradiation of the amorphous-crystalline boundaries has been associated with a *reduction* of the *effective amorphization threshold* due to the defects created by prior irradiation (*cumulative damage*). The kinetics of the two boundaries of the buried layer is quite different, suggesting that other mechanisms aside from the electronic stopping power should play a role on ion-beam damage.
 [DOI: 10.1063/1.2434801]

I. INTRODUCTION

Ion-beam irradiation offers a general method to modify the structure and properties of materials with several advantages over other physical or chemical methods.[1–3] So far, the technological applications of ion irradiation mostly rely on the effects caused by nuclear collisions and ion implantation. In particular, ion implantation of transparent materials with light ions (H and He) has allowed for the fabrication of optical waveguides and a variety of integrated optical devices although at the expense of quite high fluences (10^{16}–10^{17} at./cm^2). Recently, a growing interest is being paid to the material modifications induced by high-energy medium mass ions (*swift-heavy ions*) where electronic excitation is dominant over nuclear collisions. There is evidence[4–9] that heavy lattice damage and even amorphization are induced by single ion impacts in dielectric crystals when the electronic stopping power S_e is above a certain *intrinsic threshold* S_{eh} that is characteristic of the material. The generated linear "amorphous" regions surrounding the ion trajectory are designated as *latent tracks*. The diameter of the tracks is around a few nanometers and steadily increases with stopping power above threshold. So, the method offers a way to devise in a controlled manner a variety of nanostructures and nanopatterns in solids.[10] On the other hand, with subthreshold irradiations ($S_e < S_{eh} \approx 5$ keV/nm) and using high enough fluences, a heavily damaged and/or amorphous surface layer has been very recently achieved on $LiNbO_3$ by oxygen,[11–14] fluorine,[14] and nitrogen[14] irradiations with energies around 5 MeV, as well as by silicon irradiations[13,15] at 5, 7.5, and 30 MeV. One attractive feature of those experiments for material processing is that the electronic excitation method requires much lower irradiation fluences for lattice damage and amorphization (around 10^{13}–10^{14} at./cm^2 for silicon beams) in comparison with nuclear collisions and generates impurity-free layers. Moreover, it offers other possibilities for tailoring refractive index profiles and so optical performance. In fact, a low-loss steplike surface waveguide, confined by a buried low refractive index damaged layer, has recently been generated[16] in a $LiNbO_3$ crystal by irradiating with F ions at 22 MeV. However, the nature and mechanisms of the electronic excitation damage have been less explored and are poorly known. Therefore, a deeper characterization of electronic damage is

[a)]Author to whom correspondence should be addressed; electronic mail: j.olivares@io.cfmac.csic.es
[b)]Present address: CELLS, 08193 Bellaterra, Barcelona, Spain.
[c)]Also at Depto. de Física de Materiales C-IV, Universidad Autónoma de Madrid, E-28049 Madrid, Spain.

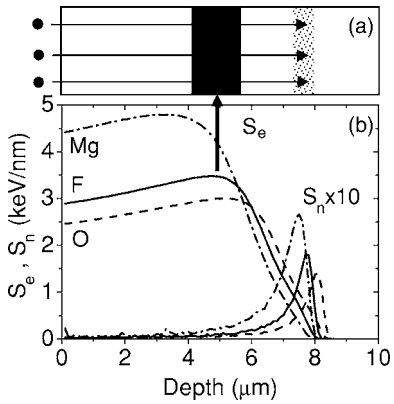

FIG. 1. (a) Plot of the electronic and nuclear stopping power curves for F at 22 MeV (continuous lines), O at 20 MeV (dashed lines), and Mg at 28 MeV (dashed-dotted lines); (b) illustrative scheme of the generated buried amorphous layer (black strip) near the maximum of the electronic stopping curves. The dotted strip indicates the region of nuclear damage and implantation.

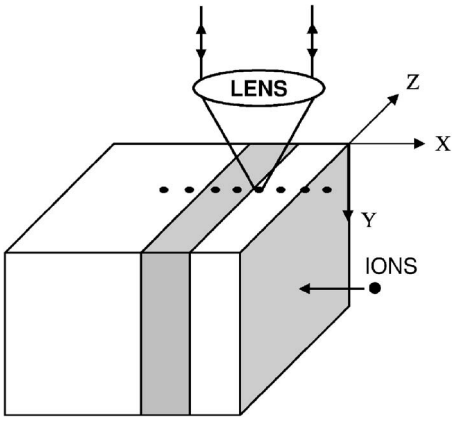

FIG. 2. Experimental configuration for observation of Raman spectra looking on a polished *Y*-cut cross section. Irradiation is along the *X* direction.

necessary in order to exploit the expected potential of swift ions.

Stimulated by our previous work,[16] the purpose of this paper is to investigate in detail the formation of buried amorphous layers by electronic excitation under diverse ion-beam irradiation conditions. The dark-mode data to measure refractive indices have been complemented with optical spectroscopy techniques (micro-Raman and second-harmonic generation) together with Rutherford backscattering spectroscopy (RBS)/channeling. The main objective has been to determine the structural profiles of the damaged and amorphous layers and investigate the dynamics of the crystalline-amorphous layers under irradiation. This information has provided relevant clues to learn about the physical processes (scarcely known so far) acting under irradiation in the electronic excitation regime. The thermal stability of the buried layers has been tested up to 300 °C. Experiments have been performed on $LiNbO_3$, since it is a reference material[17,18] for electro-optic and nonlinear optical applications and constitutes an adequate substrate for fabrication of high-quality waveguides. However, the method could be, in principle, extended to any crystalline transparent material.

II. EXPERIMENTAL METHODS

The strategy followed in these experiments is illustrated in Fig. 1. One looks for irradiation conditions where the maximum of the $S_e(z)$ curve lies at a certain depth inside the crystal [well separated from the peak value of the nuclear stopping power $S_n(z)$] and reaches a value close to the intrinsic threshold ($S_{eh} \approx 5$ keV/nm). Our irradiation conditions for F at 22 MeV, O at 20 MeV, and Mg at 28 MeV fulfill this requirement as illustrated in Fig. 1(a), derived from SRIM 2003 calculations.[19] Then, it is expected that, after some critical fluence, amorphization at every single ion trajectory starts at the location of the maximum of $S_e(z)$, so that the process would proceed as illustrated in Fig. 1(b): When the fluence guarantees full overlapping of the individual latent tracks ($\sim 10^{13}$ at./cm^2), a low refractive index homogeneous layer is formed inside the crystal and consequently a planar optical waveguide is generated at the surface.

X- and *Z*-cut nominally pure (integrated optical grade) $LiNbO_3$ plates purchased from Photox Optical Systems, UK, were irradiated at random incidence with O^{+4} (20 MeV), and F^{+4} (22 MeV), and Mg^{6+} (28 MeV) ions in the 5 MV Tandetron accelerator recently installed at the CMAM in the University Autónoma de Madrid.[20] Ion-beam currents were in the range of 10–50 nA to prevent excessive charging and heating. Samples were tilted 9° with respect to beam direction to avoid ion channeling. The dimensions of the irradiated area were typically 6×6 mm^2.

The refractive index profiles induced by irradiation have been determined by the prism-coupling dark *m*-line method using a 5 mW He–Ne laser at $\lambda = 632.8$ nm.

To characterize the damage layer and learn about its formation kinetics, RBS/channeling and Raman techniques were used. The RBS/channeling experiments were performed around the *c*-axis channel using H ions at 3 and 3.8 MeV.

Raman spectra were recorded with a Renishaw Ramascope 2000 microspectrometer and an argon ion laser operating at a wavelength of 514.5 nm. The power on the sample was kept below 5 mW. In order to get the best spatial resolution, the spectra were collected from an optical grade polished cross section of the sample, as illustrated in Fig. 2. The same configuration was used to take microphotographs under reflected light. In these conditions, lateral spatial resolution is about 1 μm (limited by light diffraction).

On the other hand, in order to gain information on the initial stage of damage, the second-harmonic response of the crystalline surface layer was evaluated by using the method described in Ref. 21 in a reflection geometry. For the fundamental beam, we use the 532 nm output of a frequency-doubled Nd:YAG (yttrium aluminum garnet) laser. It was focused on the surface of the plate to an intensity of 10^{12} W m^{-2}. In order to probe the d_{33} coefficient in *Z*-cut samples, the incidence beam formed an angle of 45° with the optical axis and its polarization was parallel with the incident plane. This generates a second-harmonic (SH) beam at 266 nm that lies well inside the ultraviolet (UV) absorption edge of $LiNbO_3$ (≈ 320 nm) and is detected in a reflection geometry. To minimize photorefractive degradation and

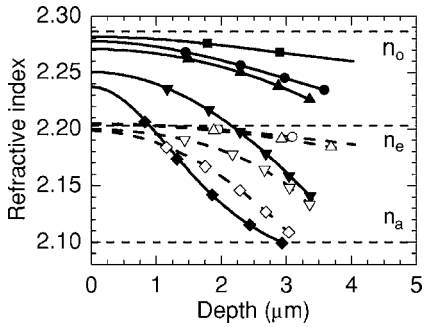

FIG. 3. Ordinary (full symbols/continuous lines) and extraordinary (open symbols/dashed lines) refractive index profiles ($\lambda = 633$ nm) for 28 MeV Mg irradiations at different fluences: 4×10^{12} at./cm^2 (squares), 8×10^{12} at./cm^2 (circles), 1×10^{13} at./cm^2 (up triangles), 2×10^{13} at./cm^2 (down triangles), and 3×10^{13} at./cm^2 (rhombi). The symbols mark the corresponding effective refractive indices. The corresponding refractive indices (n_o and n_e) for crystalline $LiNbO_3$ as well that one (n_a) for amorphous material are marked on the plot.

beam fanning, relatively low incident light powers were used. Note that due to the strong absorption of the crystal at 266 nm, the method only provides information about a thin surface layer of around 50 nm in thickness.

III. RESULTS

A. Refractive index profiles

The refractive index profiles were obtained from the dark-mode data either through a WKB code or by direct fitting to Fermi-type curves. The two methods yield consistent results for the relevant parameters, waveguide thickness, and upper and lower levels of the index well. With increasing irradiation fluence, the two refractive indices (ordinary and extraordinary) decrease markedly inside the crystal, whereas, at low fluences, their values at the surface remain relatively close to that of bulk $LiNbO_3$. Data are illustrated in Fig. 3 for Mg irradiations at 28 MeV. One should note, however, that a small initial increase is observed for the extraordinary index accompanied by an even smaller decrease in the ordinary index. In all cases the heavy-damage process starts at a certain depth beneath the surface near the position of the maximum of the $S_e(z)$ curve (e.g., around 3.5 μm for Mg). For sufficiently high fluences, the profile approaches a steplike shape, whose bottom level reaches a limit value, $n=2.10$, approximately independent of the investigated ions as well as of light polarizations and coincides with the refractive index of amorphous $LiNbO_3$.[15,22] The profiles reached at this stage for F, Mg, and O irradiations are comparatively illustrated in Fig. 4. They are quite sharp for F and O but smoother and closer to the surface for Mg. Anyhow, they accept a high number of propagating modes ($\geqslant 10$) for both ordinary and extraordinary polarizations in accordance with a large index jump, close to 0.1 for n_e and 0.2 for n_o. The presence of the buried amorphous layer is clearly illustrated in the microphotographs of Fig. 5, corresponding to F-irradiated samples.

Another relevant outcome of our results (see Fig. 5) is that the thickness of the amorphous layer increases with irradiation fluence due to the propagation of the two boundaries. The outer high-energy (h) boundary moves towards the sample surface, whereas the inner low-energy (l) boundary moves deeper into the crystal. The dark-mode data give information about the outer boundary, whereas the kinetics of the inner boundary requires other techniques, particularly RBS/channeling to be discussed below.

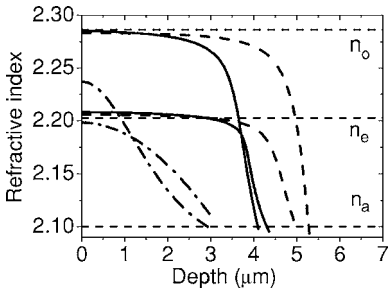

FIG. 4. Refractive index profiles for samples irradiated with 22 MeV F at a fluence of 2×10^{14} at./cm^2 (continuous lines), with 20 MeV O at 6×10^{14} at./cm^2 (dashed lines), and with 28 MeV Mg at 3×10^{13} at./cm^2 (dashed-dotted line).

Although the behavior found for all ions is qualitatively similar, the F irradiation experiments covered higher fluences. For this case, the depth of the outer h boundary is plotted as a function of fluence in Fig. 6 (the information for the l boundary, also plotted, has been derived from RBS spectra discussed in Sec. III B). The rate of motion in fluence units is, initially, fast but then slows down and tends to a rather steady value. The data point corresponding to the lowest fluence indicates a boundary depth of around 4 μm to be compared with the position of the maximum of S_e at 4.7 μm.

B. RBS/channeling data

In order to obtain information on the inner l boundary of the amorphous layer and additional data on the outer h boundary, detailed RBS/channeling data have been taken for

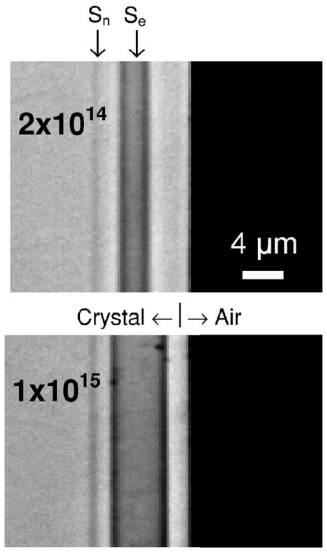

FIG. 5. Optical microphotographs (geometry of Fig. 2) of a polished Y-cut cross section for samples irradiated with F at fluences of 2×10^{14} and 1×10^{15} at./cm^2. The depths of the maximum electronic stopping power (S_e) and of the nuclear stopping power (S_n) are indicated with arrows. Note also a faint line corresponding to the region of nuclear damage (end of ion range).

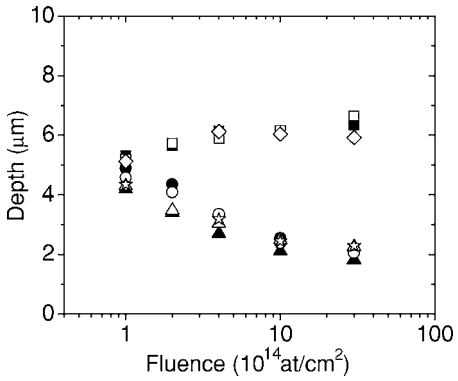

FIG. 6. Depth location for the *l* and *h* boundaries of the amorphous layer in F-irradiated samples (22 MeV) as a function of fluence. Open symbols correspond to samples just after irradiation. The data for the *h* boundary are dark mode (circles), RBS/channeling (triangles), and micro-Raman (stars). For the *l* boundary, RBS (squares) and micro-Raman (rhombi) data are shown. Data obtained after annealing at 300 °C (full symbols) are also included.

samples irradiated with F and Mg beams at several fluences. One sees from the spectra displayed in Fig. 7(a) (for F irradiations) and Fig. 7(b) (for Mg irradiations) that at fluences above 10^{14} at./cm^2, a buried region with randomlike yield is observed. On the other hand, in accordance with the optical data, a surface (waveguiding) layer remains with slightly disturbed channeled spectra and so good crystalline quality. Moreover, some differences appear between the two cases (F and Mg) that are in accordance with those optically observed, namely, wider waveguiding layers at equal fluence for F irradiations. Moreover, in this case, the *h* boundary, separating the outer crystalline from the buried amorphized layer, is quite sharp in agreement with the dark-mode data. Its depth location as a function of fluence, plotted for comparison in Fig. 6, follows the same trend as that found from the measured dark modes although it appears at somewhat smaller values (see Sec. V). Anyhow, in both cases, the transition from the crystalline to the amorphous phase occurs rather abruptly after reaching a certain level of disorder (≈20% degree of amorphization). On the other hand, the *l* boundary of the amorphous layer moves deeper into the crystal on increasing fluence. For F irradiations, where spectra are better defined, its approximate depth positions are also included in Fig. 6 (note that for this boundary, information from dark modes cannot be obtained). This boundary appears smoother (see Fig. 7) in comparison with the outer one, possibly due to dechanneling effects produced in the heavily distorted amorphous layer.

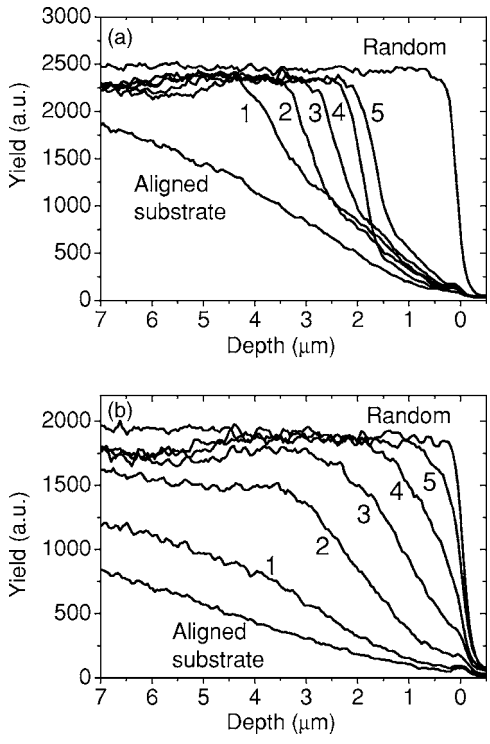

FIG. 7. (a) RBS/channeling spectra along the *c* axis for samples irradiated with F (22 MeV) using H at 3 MeV as probing ion. Fluences are 1×10^{14} at./cm^2 (1), 2×10^{14} at./cm^2 (2), 4×10^{14} at./cm^2 (3), 1×10^{15} at./cm^2 (4), and 3×10^{15} at./cm^2 (5). (b) RBS/channeling spectra along the *X* axis for samples irradiated with Mg (28 MeV) using H at 3.8 MeV as probing ion. Fluences are 1×10^{12} at./cm^2 (1), 2×10^{12} at./cm^2 (2), 1×10^{13} at./cm^2 (3), 2×10^{13} at./cm^2 (4), and 3×10^{13} at./cm^2 (5).

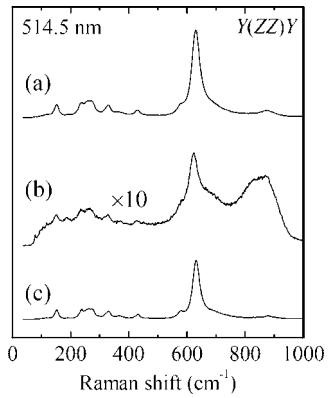

FIG. 8. Raman spectra $[Y(ZZ)Y]$ for a F-irradiated sample (22 MeV) at a fluence of 3×10^{15} at./cm^2. Spectra correspond to (a) surface (waveguide) layer, (b) amorphous (barrier) layer, and (c) substrate.

C. Raman data

Fluorine irradiated samples were probed with micrometer resolution at different layer depths by micro-Raman spectroscopy. Spectra were taken at different points along a line parallel to the *X* crystal axis on a polished *Y*-cut cross section (see Fig. 2). The incident and scattered light were propagating along the *Y* direction. The different spectra corresponding to the outer waveguiding layer, the buried heavily damaged optically isotropic layer, and the substrate are represented in Fig. 8 for the polarization geometry $Y(ZZ)Y$ in Porto notation. The spectra for the outer layer and the substrate show sharp peaks that are characteristic for first-order Raman scattering and closely correspond to those reported[23] for crystalline $LiNbO_3$. On the other hand, a much reduced Raman yield and broad band profiles at 630 and 830 nm are observed in the buried layer, suggesting a strong structural disorder. In fact, those broad features are similar to those observed in $LiNbO_3$ that has been amorphized by different procedures.[24,25] However, clear remnants of the narrow peaks typical of crystalline $LiNbO_3$ are also apparent, indicating that some crystalline regions survive and are embed-

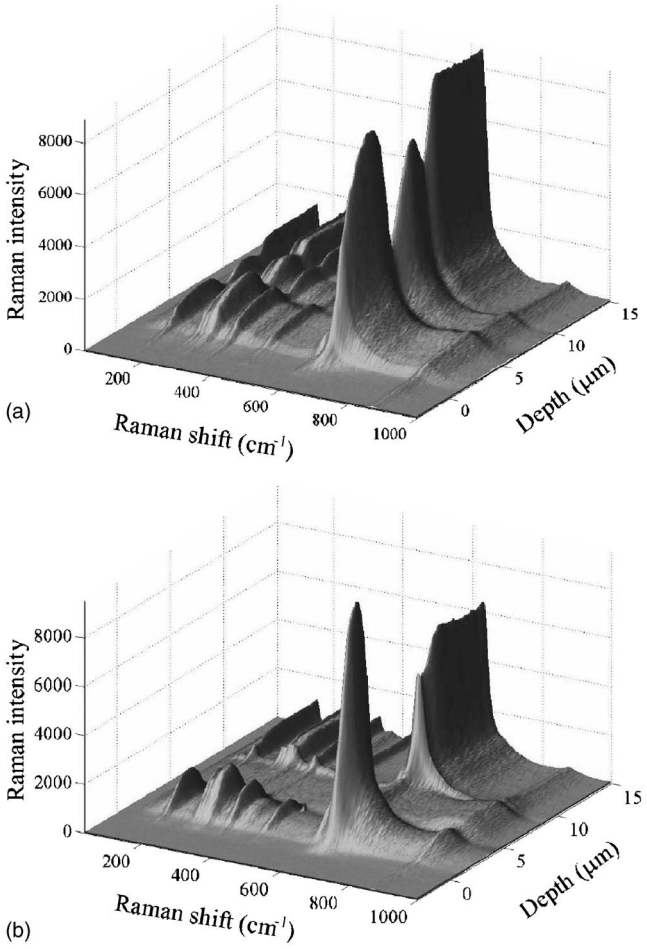

FIG. 9. Raman spectra as a function of layer depth for F-irradiated *Z*-cut samples (22 MeV). Configuration geometry was [*Y*(*ZZ*)*Y*]. Fluences were (a) 1×10^{14} at./cm^2 and (b) 3×10^{15} at./cm^2

ded into the amorphous phase. The fraction of such regions can be estimated to be around 5% from the spectra in Fig. 8. It is to be noted that the positions of the crystalline peaks are slightly shifted to lower wavelengths in comparison with those of the substrate (and outer layer). This may be a consequence of the lattice expansion of the crystals in a low density phase.

The evolution of the spectra with depth is well illustrated by the three-dimensional plots of Fig. 9 for *Y*(*ZZ*)*Y* configuration and fluences of 1×10^{14} at./cm^2 [Fig. 9(a)] and 3×10^{15} at./cm^2 [Fig. 9(b)]. On increasing depth, it shows the sequence, crystalline-amorphous-crystalline phases, that reproduces faithfully the pattern observed in the pictures of Fig. 5 and the data obtained by the dark-mode technique. There is also a small dip in the Raman intensity at a depth of about 8 μm, which lies well inside the crystalline substrate. This feature probably corresponds to the damaged layer associated with the nuclear stopping at the end of the ion range (see faint feature in Fig. 5). It is remarkable that the spectra in the crystalline surface layer show a higher yield than those measured deep in the crystalline substrate. This is probably due to the light concentration effects caused by waveguiding and the finite size of the sample. The thickness of the waveguiding layer may be derived from the first derivative of a plot showing the total Raman intensity as a function of

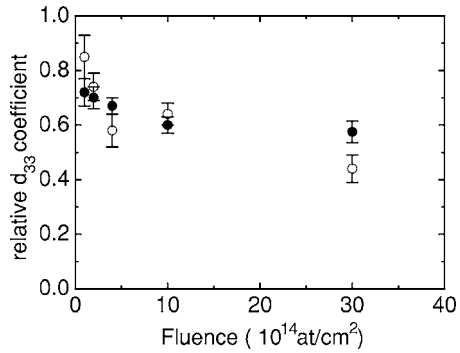

FIG. 10. SHG yields normalized to that of the unirradiated crystal for the surface (waveguiding) layer of F-irradiated samples (22 MeV) as a function of fluence (open symbols). The data corresponding to samples annealed at 300 °C, after irradiation, are shown for comparison (full symbols).

depth or its first and second derivatives. Unfortunately, the depth resolution (between 1 and 2 μm) is much worse than that achieved with the dark-mode data. Anyhow, the results obtained after averaging the data from several samples (also included in Fig. 6) are quite consistent with those derived from the dark-mode method and RBS/channeling spectra.

D. Second-harmonic generation (SHG) data

In order to obtain additional information on the structural quality of the crystalline top layer (where no amorphization has been induced) and assess the potential of the steplike waveguide for nonlinear optics (NLO) applications, the SHG response of the layer has been measured as a function of fluence. First of all, the SHG yield for the various fluences (and for a reference, virgin $LiNbO_3$ sample) was measured as a function of the fundamental light intensity, in order to assess the intensity region where a quadratic dependence applies. This allows to determine a meaningful value of the relative second-harmonic susceptibility d_{33}. The data are plotted in Fig. 10. For the F irradiations, the SHG susceptibility at the crystal surface shows an initial rapid decrease at low fluences and reaches around ≈60% of the bulk value of unirradiated $LiNbO_3$ for fluences around or above 10^{15} at./cm^2. For the O irradiations, some measured data show that the susceptibility decays down to around 60%–70% of the bulk value after a fluence of $\sim3\times10^{15}$ at./cm^2. The reason for the fast initial decrease in SHG yield is not clear. It may be associated with the lattice defects created during the preamorphization stage and so may be related to the small changes in the extraordinary refractive index at the surface (shown in Fig. 3). Anyhow, a similar effect observed in ion implanted $LiNbO_3$ has been attributed to depoling caused by the irradiation.[26]

IV. EFFECT OF THERMAL ANNEALING

The effect of thermal annealing after irradiation has been investigated up to 300 °C. In this temperature range, all main features are preserved. The refractive index profiles are not essentially modified although they become sharper, allowing for a better definition of boundary locations. As an example, the effect of annealing is illustrated in Fig. 11 for the fluorine irradiations. The same behavior is observed in

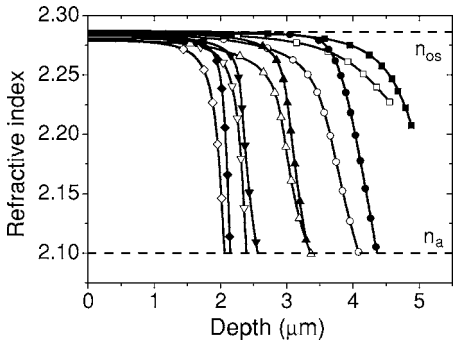

FIG. 11. Effect of annealing at 300 °C on the ordinary refractive index profiles of F-irradiated (22 MeV) *Z*-cut samples. Open symbols correspond to the as-irradiated samples and full symbols to the annealed samples. Fluences (in units of at./cm^2) are 1×10^{14} (squares), 2×10^{14} (circles), 4×10^{14} (up triangles), 1×10^{15} (inverted triangles), and 3×10^{15} (rhombi). The substrate (n_{os}) and amorphous $LiNbO_3$ (n_a) refractive index values are indicated with dashed lines for reference.

the RBS/channeling spesctra. In fact, the depth values show some small variations but do not indicate a significant effect of the annealing treatment. The positions of both the *l* and *h* boundaries after annealing have been included in Fig. 6. Similarly, the relative SHG coefficients after annealing do not show significant changes in comparison with those prevailing just after irradiation (see Fig. 10). The main effect is the removal of color centers generated by the irradiation and the great enhancement of the transparency. The consequence is a rather low level of losses measured in the F-irradiated and annealed waveguides that reaches values[16] around 1 dB/cm.

V. DISCUSSION

A. Damage kinetics and mechanisms: Thresholding

Key questions to be answered are the mechanisms responsible for the irradiation-induced damage, its evolution with fluence, and the structure of the damaged regions. With regard to the first question, one sees from Figs. 3, 4, and 9 that the refractive index and Raman profiles are not at all correlated with the nuclear damage distribution obtained by SRIM2003 simulations shown in Fig. 1. Moreover, the depth at which the amorphous region starts very approximately coincides with the position of the maximum of the electronic stopping power curve in Fig. 1. Therefore, one can safely conclude that electronic excitation mechanisms mostly account for the lattice damage which appears to be correlated with the stopping power curve $S_e(z)$.

All spectroscopic data, in particular, RBS/channeling (Fig. 7), show that electronic damage is cumulative and one can distinguish two different stages. A first stage, hereon termed *preamorphization stage*, involves a relatively low level of damage, very likely constituted by point defects, which is followed by an abrupt transition to a stage of heavy damage usually characterized as *amorphization stage* (see below). In the preamorphization stage, one sees small changes in the two refractive indices as well as in the Raman spectrum. The RBS spectra, as a function of fluence, show that the generated defects in such stage produce an increasing degree of dechanneling of the H beam up to a point where the backscattering yield rather abruptly reaches the random value representative of the final amorphous stage. In other words, the transition from one stage to the other is *abrupt*, as also evidenced by the sharp refractive index and Raman intensity profiles. The behavior is indicative of a definite *threshold* in the electronic stopping power S_e needed to achieve the amorphization. It should correspond to the critical defect concentration required to start a phase transition and make the lattice collapse. One may expect that this threshold is related to that one measured for the generation of isolated single tracks in virgin (unirradiated) crystals. For $LiNbO_3$ the reported values for such intrinsic threshold in a virgin sample are between 4 and 6 keV/nm, so that no amorphization is, in principle, expected for the F (22 MeV) irradiations and O (20 MeV) where the maximum S_e is around 3 keV/nm. Our present data show that a certain critical fluence ($\sim10^{14}$ at./cm^2) has to be given to the sample in order to reduce the threshold to an effective value equal to such maximum S_e (3 keV/nm) and so start amorphization. In conclusion, our study confirms the existence of a fluence-dependent effective stopping power threshold, $S_{\mathrm{th}}^{\mathrm{eff}}$. For virgin (unirradiated) samples, it should coincide with that measured in single-track experiments. The dependence on fluence is not surprising as long as the defects generated by irradiation should reduce the number of additional defects needed for lattice collapse to an amorphous phase.

The above concept of a fluence-dependent effective threshold immediately accounts for the motion of the crystalline-amorphous boundaries on increasing irradiation, nicely illustrated by the data of Fig. 6. The above ideas have been substantiated by a recent theoretical model[27,28] based on the *thermal spike concept* and on the *cumulative character* of the damage. The model assumes that the defect concentration generated at a given depth by a single impact is exclusively determined by the deposited energy $S_e(z)$ and corresponds to thermal equilibrium at the maximum temperature locally reached in the spike.[27] The total depth concentration can then be calculated by numerical integration[27,28] as a function of the accumulated fluence, assuming that the intrinsic threshold S_{th} is known. When such concentration reaches a certain critical value at the considered depth *z*, an abrupt transition to the amorphous state occurs. In this situation, the electronic stopping power $S_e(z)$ at that layer can be identified with the above-defined *effective threshold* $S_{\mathrm{th}}^{\mathrm{eff}}$. The model was able to approximately account for the data on the depth location of the amorphous-crystalline boundary as a function of fluence under silicon irradiations at 5 and 7.5 MeV using an intrinsic threshold of 5 keV/nm and a thermal formation energy of 0.6 eV.

B. Motion of boundaries

The present experiments using high-energy F irradiations show specific features in comparison with those previously performed with silicon.[13,15] First, in the case of F irradiations, there are two crystalline-amorphous boundaries that lie at different sides of the stopping power maximum (see Fig. 1). Both of them move upon irradiation in the direction of the lower stopping powers, i.e., the outer *h* boundary to-

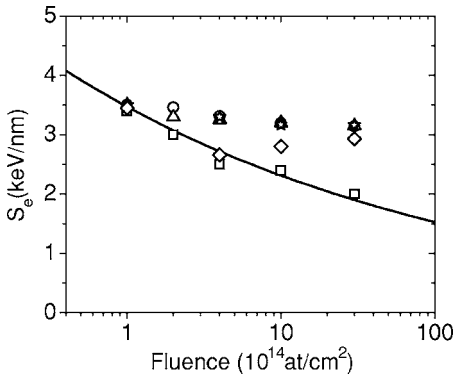

FIG. 12. Experimental data (from Fig. 6) showing the electronic stopping power S_e at the boundaries as a function of fluence. The data for the h boundary are dark mode (circles), RBS/channeling (triangles), and micro-Raman (stars). For the l boundary, RBS (squares) and micro-Raman (rhombi) data are shown. The line corresponds to a model calculation using S_{th}=7 keV/nm, a_0=4.5 nm, and kT_m/ε=0.2.

wards the surface whereas the inner one l boundary propagates deeper into the crystal. To quantify the comparison between the two boundaries, we have plotted in Fig. 12 the data from Fig. 6 but substituting now the electronic stopping power S_e for the corresponding boundary depth (see the SRIM curves in Fig 1). According to the model,[27] schematically described in the previous section, the curves showing the fluence evolution of either one of the boundaries should show the *same universal* kinetic behavior in the $S_e(\phi)$ plot. One clearly sees that this is not the case. The slope of the $S_e(\phi)$ curve, and so the efficiency of defect creation, appears to be smaller for higher energies than that achieved at lower energies, the stopping power being equal. In other words, the defect creation rate (or damage cross section) decreases with increasing ion velocity or energy per atomic mass unit (the so-called *velocity effect*[29,30]). In fact, the data for the l boundary in Fig. 12 can be fitted to the model using an intrinsic threshold S_{th} of 7 keV/nm, somewhat higher than that used for Si.[27] On the other hand, the data for the h boundary cannot be fitted for any reasonable value of S_{th}. It is worth remarking that the velocity effect has been, so far, inferred from a comparison of the effects of *different ions or molecular clusters* in single impact experiments. Our experiments may provide the first comparison using the *same* ion in two different stopping power regimes. A complete analysis is premature at this stage, since the available data are scarce and scattered. Other effects that one might consider in a full analysis include the role of the external surface, nuclear collisions, induced changes in lattice stress, and crystal density.

C. Structural considerations

With regard to the structure of the amorphous layer, some relevant comments are in order. First, one should remark that it corresponds to a material having an isotropic refractive index (n=2.10) that is quite robust, i.e., that is not modified by further irradiation. Moreover, the value is the same for our O, F, and Mg irradiations as well as for irradiations with other ions such as Si in the electronic loss regime. This is also the case for high-fluence irradiations with light ions (H and He), where nuclear losses are dominant.[3,22] On the other hand, the heavily damaged region presents a very faint Raman spectrum, consisting of weak remnants of the sharp peaks of the crystalline phase on top of a relatively large background and with broad features at 630 and 830 cm^{-1} which have been previously associated with amorphous $LiNbO_3$ produced by different physicochemical methods.[24,25] They have been associated with distorted and/or defective oxygen octahedra with partial oxygen deficiency. Finally, RBS/channeling data show a fully random yield along the c axis, indicating a heavily distorted crystallographic channel. In conclusion, all those features support the consideration of amorphous for the buried heavily damaged layer produced by our F, O, and Mg irradiations. Unfortunately, the experiments reported in this paper do not provide specific information on the atomic arrangements in the amorphous phase. However, the Raman data suggest that the basic structural units (oxygen octahedra) are preserved during the preamorphous stage of irradiation, although they may become rotated and/or distorted and defective. This idea is consistent with the evidence that those octahedral units show a high structural stability and robustness in perovskite related oxides.[31,32]

The SHG experiments give some clues on the structure of the preamorphization stage. Irradiation rapidly introduces lattice distortions that slightly modify both the ordinary and extraordinary refractive indices at the surface (Figs. 3 and 4) and reduce the SHG yield (Fig. 10). The same effects have been observed after low-fluence ion implantation[3,21] and attributed to the decrease in the spontaneous polarization caused by the irradiation-induced lattice defects. The electronic configuration of those defects (i.e., the formation of color centers) is not much relevant for the observed effects, as inferred from the minor role of thermal annealing.

VI. SUMMARY AND CONCLUSIONS

The relevant outcome of this work is the generation in $LiNbO_3$ of an optically isotropic low-index (amorphous) layer beneath the surface by using different swift-ion beams. The amorphous structure of such layer has been assessed by complementary spectroscopic techniques, including Raman scattering and RBS/channeling. One should note that at variance with the amorphization induced by conventional ion implantation, our amorphous layer is *free* of impurities (implanted ions). On the other hand, the process approximately maintains the refractive index values of the bulk crystal in the surface layer, so allowing for the propagation of highly confined modes. The inner amorphization is generated by electronic excitation damage using an adequate $S_e(z)$ curve that overcomes the threshold value inside the crystal. The amorphization process starts at the location of the maximum of the $S_e(z)$ curve and can be controlled by a suitable choice of the bombarding ion, fluence, and energy. The boundaries separating the crystalline and amorphous layers move towards the regions of smaller S_e with increasing fluence. This suggests that the threshold stopping power to start lattice amorphization decreases on prior irradiation in accordance with a cumulative character of the electronic damage as found in previous experiments with silicon beams. The re-

sults presented in this paper provide significant information (and stimulus) for a better understanding of the physical mechanisms causing lattice damage and amorphization in $LiNbO_3$.

[1] *Ion Implantation-2000: Science and Technology*, edited by J. F. Ziegler (Lattice, Sunset Beach, CA, 2000).
[2] M. Nastasi, J. W. Mayer, and J. K. Hirvonen, *Ion-Solid Interactions: Fundamentals and Applications* (Cambridge University Press, Cambridge, 1996).
[3] P. D. Townsend, P. J. Chandler, and L. Zhang, *Optical Effects of Ion Implantation* (Cambridge University Press, Cambridge, 1994).
[4] R. L. Fleischer, P. B. Price, and R. M. Walker, *Nuclear Tracks in Solids* (University of California Press, Berkeley, 1975).
[5] M. Toulemonde, S. Bouffard, and F. Studer, Nucl. Instrum. Methods Phys. Res. B **91**, 108 (1994).
[6] E. Ferain and R. Legras, Nucl. Instrum. Methods Phys. Res. B **174**, 116 (2001).
[7] G. Szenes, Phys. Rev. B **51**, 8026 (1995).
[8] R. Spohr, in *Ion Tracks and Microtechnology: Basic Principles and Applications*, edited by K. Bethge (Vieweg, Braunschweig, 1990).
[9] M. Toulemonde, C. Trautmann, E. Balanzat, K. Hjort, and A. Weidinger, Nucl. Instrum. Methods Phys. Res. B **216**, 1 (2004).
[10] J. Olivares, A. García-Navarro, G. García, A. Méndez, and F. Agulló-López, Appl. Phys. Lett. **89**, 071923 (2006).
[11] G. G. Bentini *et al.*, J. Appl. Phys. **92**, 6477 (2002).
[12] G. G. Bentini *et al.*, J. Appl. Phys. **96**, 242 (2004).
[13] J. Olivares, G. García, F. Agulló-López, F. Agulló-Rueda, J. C. Soares, and A. Kling, Nucl. Instrum. Methods Phys. Res. B **242**, 534–537 (2006).
[14] M. Bianconi *et al.*, Appl. Phys. Lett. **87**, 072901 (2005).
[15] J. Olivares, G. García, F. Agulló-López, F. Agulló-Rueda, A. Kling, and J. C. Soares, Appl. Phys. A: Mater. Sci. Process. **A81**, 1465 (2005).
[16] J. Olivares, G. García, A. García-Navarro, F. Agulló-López, O. Caballero, and A. García-Cabañes, Appl. Phys. Lett. **86**, 183501 (2005).
[17] *Properties of Lithium Niobate*, EMIS Datareview Series, Edited by K. K. Wong (INSPEC, Exeter, 2002).
[18] F. Agulló-López, J. M. Cabrera, and F. Agulló-Rueda, *Electrooptics: Phenomena, Materials and Applications* (Academic, London, 1994).
[19] *The Stopping and Ranges of Ions in Solids*, edited by J. F. Ziegler, J. P. Biersack, and U. Littmark (Pergamon, New York, 1985); see also the SRIM web page, http://www.srim.org
[20] D. J. W. Mous, A. Gottdang, R. G. Haitsma, G. García López, A. Climent-Font, F. Agulló-López, and D. O. Boerma, Proceedings CAARI 2002; see also www.uam.es.cmam
[21] J. Rams and J. M. Cabrera, J. Mod. Opt. **47**, 1659 (2000).
[22] G. L. Destefanis, J. P. Gailliard, E. L. Ligeon, S. Valette, B. W. Farmery, P. D. Townsend, and A. Perez, J. Appl. Phys. **50**, 7898 (1980).
[23] R. F. Schaufele and M. J. Weber, Phys. Rev. **152**, 705 (1966).
[24] Y. Lin, Y. Li, Y. Xu, G. Lan, and H. Wang, J. Appl. Phys. **77**, 3584 (1995).
[25] S. H. Kim, S. J. Lee, J. P. Kim, B. G. Chae, Y. S. Yang, and M. S. Jang, J. Korean Phys. Soc. **32**, S830 (1998).
[26] J. Rams, J. Olivares, P. J. Chandler, and P. D. Townsend, J. Appl. Phys. **84**, 5180 (1998).
[27] F. Agulló-López, G. García, and J. Olivares, J. Appl. Phys. **97**, 093514 (2005).
[28] G. García, F. Agulló-López, J. Olivares-Villegas, and A. García-Navarro, J. Appl. Phys. **99**, 1 (2006).
[29] T. A. Tombrello, Nucl. Instrum. Methods Phys. Res. B **94**, 424 (1994).
[30] A. Meftah, J. M. Constantini, N. Khalfaoui, S. Boudjadar, J. P. Stoquert, F. Studer, and M. Toulemonde, Nucl. Instrum. Methods Phys. Res. B **237**, 563 (2005).
[31] A. M. Glazer, Acta Crystallogr., Sect. B: Struct. Crystallogr. Cryst. Chem. **28**, 3384 (1972).
[32] A. M. Glazer, Acta Crystallogr., Sect. A: Cryst. Phys., Diffr., Theor. Gen. Crystallogr. **31**, 756 (1975).